Nonlinear Gyrofluid Models of Shear Alfvén Instabilities in Ignited and Beam Heated Toroidal Plasmas

D. A. Spong, C. L. Hedrick, B. A. Carreras
Oak Ridge, TN 37831-8071
Oak Ridge National Laboratory *

Abstract

Shear Alfvén instabilities driven by energetic beams and alpha populations are investigated using a reduced MHD-gyrofluid model with Landau closure. The moment equations for the fast ions are truncated in a way which incorporates the wave particle resonances that are required to destabilize the shear Alfvén mode. These are coupled to an Ohm's law and vorticity equations which have been generalized to include ion FLR, electron and ion Landau damping. This model has been applied to experimentally observed regimes in a number of tokamak and stellarator devices. Both linearized growth rates and the nonlinear evolution are obtained. The saturated nonlinear regimes indicate mode number and frequency spectra which are generally consistent with experiment. A detailed examination of one typical nonlinear state has allowed identification of the dominant saturation mechanisms. This indicates that generation of n=0, m=0 sheared poloidal velocity flows and quasi linear modification of the q(r) profile can be important factors in reaching saturation.

I. Introduction

Large tokamak experiments will soon begin operation using D-T fuel mixtures in order to test the physics of alpha populations. Due to their super-Alfvénic velocities, alphas can readily destabilize discrete shear Alfvén modes, leading to enhanced fast particle losses. Such instabilities have already been observed in experimental regimes at low magnetic fields where the velocities of injected beam species[1-3] or minority ion ICRF tails[4] can approach the Alfvén velocity. The gyrofluid model with Landau closure[5-7] has proven to be a promising technique for analyzing such instabilities. This approach leads to a set of coupled fluid time evolution equations which may be solved using an initial value code (TAE/FL). The equations are constructed so as to include both the wave-particle resonance effects necessary for Landau damping/growth as well as ion FLR effects. A variety of damping mechanisms which are relevant to the TAE (Toroidal Alfvén Eigenmode) instability, such as ion and electron Landau damping, and continuum damping, are also included in the equations. These damping effects are treated in a non-perturbative manner. Examples will be discussed where linear damping effects can significantly modify the spectrum of the TAE and perturbative attempts would fail to accurately represent the linear eigenmode structure. We shall first apply this model to examine the linear stability of beam-driven TAE modes in TFTR[1], DIII-D[2] and for alpha-driven TAE's in TFTR (based on extrapolations of the supershot regime to deuterium-tritium operation)[8]. The two beam-driven examples are well above the linear stability thresholds; however, the alpha-driven TFTR case is just barely above threshold. This is caused by the high ion temperatures, which result in strong ion Landau damping and the high β of the background plasma, which can enhance continuum damping. More sizable TAE growth rates may be obtained if the ion temperature is lowered.

*Research sponsored by the Office of Fusion Energy, U.S. Department of Energy, under contract DE-AC05-84OR21400 with Martin Marietta Energy Systems, Inc.

One of the primary motivations for development of the gyrofluid model is that it allows one to analyze the nonlinear behavior of the TAE instability. We have examined the nonlinear evolution for the two beam-driven TAE cases mentioned above and a reduced ion temperature TFTR alpha-driven case. Nonlinearly saturated states are generally obtained and mode number and frequency spectra are in the same range as experimental values. Significant levels of fluctuating fast ion density, and magnetic field are found in the nonlinear regime. Detailed diagnosis of the nonlinear state has recently yielded information about the saturation mechanisms which are most likely to be effective in this model. Linear growth rates have been calculated throughout the nonlinear evolution, taking into account the instantaneous n = 0, m = 0 components which are generated by nonlinear beatings of Fourier modes with the same n (toroidal mode number). Strong reductions of the resulting linear growth rates near the time where saturation is achieved indicate the important effect of this component. A further linear analysis is then performed in which the various n = 0, m = 0 field components are selectively turned on and off to isolate those which are most significant. Based on looking at a typical case (the TFTR beam-driven TAE), we find that the n = 0, m = 0 electrostatic potential (which induces sheared poloidal velocity flows) and the poloidal magnetic flux (which leads to modifications in the q-profile) account for most of the stabilization.

II. Linear Stability Studies

Our linear stability model is based on an Ohm's law, vorticity equation, and fast ion density and parallel velocity moment equations.[5] These have been generalized to include ion-electron Landau damping and ion FLR effects[7]. Effects which are not presently included in the gyrofluid model, but which may be of importance to the TAE, are: non-Maxwellian distributions, background plasma compressibility, fast ion temperature gradients, and finite fast ion orbit width effects. This model will be applied to the following three cases: (a) the TFTR beam-driven TAE experiment[1], (b) the DIII-D beam-driven TAE experiment[2], and (c) extrapolation of a TFTR supershot to operation with a 50-50 mixture of D-T[8]. The profiles and parameters used have been obtained from the associated references and will not be described in detail here. They may be briefly summarized in the following table:

Table 1 - Approximate parameters of beam and alpha driven TAE experiments

	(a) TFTR NBI	(b) DIII-D NBI	(c) TFTR-DT
$\beta_{fast}(r=0)$	0.012	0.05	0.003
$\beta_{total}(r=0)$	0.0314	0.142	0.0435
$E_{fast\ ion}$(Mev)	0.1	0.075	3.5
B_0(T)	1.0	0.789	5.1
$n_{ion}(r=0)$	3×10^{13}	4×10^{13}	4.5×10^{13}
$T_e(r=0)$	≈1 kev	2 kev	8.5 kev
$T_i(r=0)$	≈1 kev	3.3 kev	19 kev

We shall first vary a number of parameters about their nominal experimental values and examine sensitivity of the linear growth rates. These parameters are generally varied

independently to illustrate the various dependencies of interest and only the nominal operational points represent true self-consistent transport/power balance/equilibrium solutions.

First, in Figs. 1(a)-(c) the fast ion central β varied with Figs. 1(a), (b), (c) corresponding to cases (a), (b), (c), respectively, as described above. The vertical dotted lines indicate the nominal experimental operational points. The lower set of curves are the growth rates for the various n's (toroidal mode numbers) while the upper curves are the real frequencies; these are both normalized to $\tau_{Hp} = R_0 / v_{A0}$ where R_0 is the major radius and v_{A0} is the Alfvén velocity at r = 0. As might be expected, both the TFTR and DIII-D beam-driven cases [Figs. 1(a) and 1(b)], are well into the unstable regime. The dependence on beta is approximately linear as expected from simplified analytic growth rates[9]. The real frequencies tend to cluster about $\omega\tau_{Hp} = 0.33$, as is expected for the TAE mode. The DIII-D case appears to have a somewhat higher β threshold and fewer n's unstable that the TFTR case. This is possibly due to the influence of shaping; the DIII-D case had a moderate elongation of 1.6 whereas the TFTR case was circular. The alpha-driven TFTR case given in Fig. 1(c) appears to be just barely above threshold with only n = 2 and 3 having finite growth rates. The causes for this will be examined further in the following figures.

Next, in Figs. 2(a)-(c) dependence of growth rates on the mean fast ion velocity relative to the central Alfvén velocity, v_{A0}, is shown. As mentioned above, the gyrofluid model is based on a Maxwellian distribution for the kinetic species. The mean velocity here is actually the thermal velocity, which we have chosen in order to match the mean energy moment of the slowing-down distributions resulting from the experimental parameters. For the TFTR alpha-driven case [Fig. 2(c)] we have taken $\beta_{fast}(0) = 0.006$ rather than the nominal $\beta_{fast}(0) = 0.003$ in order to obtain more sizable growth rates for this particular parameter variation. As may be seen, growth rates remain significant for $< v_{beam} > / v_{A0} < 1$, especially for the higher n's and the more unstable cases. This feature is likely due to the increased sideband coupling resulting with larger n's. As more poloidal modes beyond the TAE's usual m and m+1 become significant, additional velocity resonances enter in at progressively lower velocities. Again, the TFTR beam-driven TAE [Fig. 2(a)] appears to be more strongly unstable than the other two cases.

In Fig. 3 we present a typical example of the impact of damping effects on the TAE volume averaged kinetic energy spectrum. This is based on the DIII-D beam-driven case (b). In Fig. 3(a) no damping is present while in Fig. 3(b) all damping effects (ion and electron Landau damping, ion FLR and finite β continuum damping) have been turned on. As may be seen, there is a narrowing of the spectrum and n = 1 is stabilized. This results because the damping mechanisms preferentially tend to affect the higher m's. This behavior stresses the importance of non-perturbative approaches for including TAE damping effects which self-consistently take into account effects of the damping on the eigenmode structure, such as are used in this model. Variational forms, for example, do not generally include such effects. Obtaining a consistent and accurate linear mode structure can be especially important for subsequent nonlinear calculations.

In Fig. 4 we vary only the β(central) of the plasma equilibrium, again for the DIII-D beam-driven case (b). This illustrates the stabilization of the TAE with increasing equilibrium Shafranov shift. As has been shown in ref. 10, the resulting modification of the Alfvén spectrum results in the TAE merging into the continuum as the beta limit of the background plasma is reached. Such effects will enhance continuum damping and can lessen the impact of the TAE when the background plasma is operating close to its beta limit. These effects partially account for the low growth rates of the TFTR-DT extrapolated supershot case (c).

The other factor which is significantly stabilizing for case (c) is ion Landau damping. In Figure 5 we lower the ion Landau damping rates by lowering the ion temperature (for the TFTR-DT extrapolated supershot case) and find that higher growth rates may be achieved. Techniques which would lower the ion temperature are under consideration[11] for the DT operational phase of TFTR.

III. Nonlinear Evolution of the TAE

We next turn to examine the nonlinear evolution of the three cases discussed in the previous section. In case (c) we use a reduced ion temperature [$T_i(r = 0) = 10$kev] to obtain more measurable linear growth rates. The same basic model is used, but convective nonlinearities are retained in each of the evolution equations and the magnetic nonlinearities entering into the parallel gradient operator are kept in the Ohm's law and vorticity equations. It is also necessary to keep a larger group of Fourier modes; in order to do a true nonlinear calculation, multiple n's (toroidal mode number) as well as multiple m's (poloidal mode numbers) must be retained. The necessary range of m's is determined from the linear studies, but can be estimated from the variation of the q-profile as: $nq_{min} \leq m \leq nq_{max}$. Ideally, enough n's should be kept to cover all linearly unstable modes and to provide some damped modes at high n. This can be problematical due to the rather wide range of unstable n's which can be characteristic of the TAE instability. The specific mode distributions we keep are given in the following table:

Table 2 - Fourier mode distributions used in the nonlinear runs

n	m's for case (a)	m's for case(b)	m's for case(c)
0	0 - 4	0 - 6	0 - 4
1	0 - 5	0 - 5	0 - 6
2	1 - 6	1 - 10	1 - 11
3	2 - 11	2 - 11	2 - 16
4	4 - 14	3 - 12	4 - 16
5	5 - 17	4 - 11	
6	6 - 20	5 - 12	
7		6 - 13	
8		7 - 14	

both $\sin(m\theta + n\zeta)$ and $\cos(m\theta + n\zeta)$ components are retained for all field quantities.

In Figs. 6(a) - 6(c) the nonlinear evolution of the r.m.s. averaged fluctuating potential, fast ion density, radial magnetic field and poloidal magnetic field are shown for the three cases. The r.m.s. average is performed over the mode spectrum, with the exception that the n = 0 component is excluded. These are evaluated at a local point in radius (indicated on the figures) where the mode structure is near its peak amplitude. There is generally a well-defined linear growth regime which ends with an overshoot, followed by a drop-off to a saturated phase. As may be seen, case(c) evolves over a longer timescale than cases (a) and (b) due to its lower linear growth rate; also, for case (c) it is less clear that a saturated state has been achieved. In cases (a) and (b) the fluctuating magnetic fields exceed 10^{-3} of the equilibrium field which is a typical value at which stochastic fast ion losses have been predicted to be significant.[12] For the TFTR alpha-driven case (c), the poloidal fluctuating magnetic field exceeds this level, but the radial magnetic field only transiently exceeds it. However, more recent calculations[13]

which include multiple toroidal mode numbers indicate that the stochastic loss threshold could be lower (i.e., $\delta B / B_0 \approx 2 \times 10^{-4}$). In Figs. 7(a) - 7(c) the volume-averaged perpendicular kinetic energies are plotted for the various n's. Again, similar features are observed: linear phase, overshoot, fall-off and saturated regime. In all cases, the n = 0 component (which will be important for the nonlinear saturation mechanisms discussed in the next section) eventually becomes the dominant mode in the evolution. At the next level below this, case (a) is dominated by n = 3 and 4; case (b) by n = 2 and 3; and case(c) by n = 2 and 4. In Figures 8(a) to 8(c), the fluctuating edge poloidal magnetic field is plotted vs. time. Since these have not been r.m.s. averaged, and are accumulated with a higher time resolution than the quantities of the previous two figures, they show the rapid Alfvén frequency oscillations. The modulation of the wave envelope is related to the somewhat different times that the individual n's reach saturation and the associated beatings between different modes. In Figs. 9(a) to 9(c) frequency spectra for the signals of Fig. 8 are plotted. There are generally coherent peaks at the characteristic TAE mode frequency $\omega \tau_{Hp} = 0.33$, with case (c) showing two significant peaks. Here the lower one is the fundamental TAE mode frequency and the upper one is a second harmonic, which is likely driven due to the nonlinearities. Cases (a) and (b) are close to the Mirnov frequency data obtained experimentally.[1,2]

IV. Nonlinear Saturation Mechanisms

An important motivation for the gyrofluid model is to diagnose the various saturation mechanisms which may be active for the TAE instability. One of the first suspected causes was the fast ion ejection which can be inferred from the neutron drops which were experimentally correlated[1,2] with Mirnov bursts of TAE activity. Since our model is fluid-based, it cannot readily include direct or stochastic particle losses; however, it does include fast ion density convection which leads to density profile flattening; this may be considered a fluid analog of particle ejection. Another way to address this loss is to couple the saturated field amplitudes from the gyrofluid model with Monte Carlo particle following[13] and check associated levels of particle losses. However, it is not yet clear that the enhanced particle losses associated with the TAE mode are the primary cause of the saturation or possibly just an artifact of the TAE. Since several distinct experimental TAE regimes have emerged involving both highly transient bursts of activity[1,2] as well as more steady state TAE turbulence[4], one expects the dominant saturation mechanisms will vary with regime. It is therefore desirable to examine other possibilities. In this paper we specifically study the effects of the n = 0, m = 0 components which are generated by nonlinear beatings of the n > 0 modes. These lead to: density flattening, modification of the q(r) profile, generation of sheared poloidal velocity flows, and generation of finite parallel velocity moments of the fast ion distribution. Some of the other possible saturation mechanisms are: nonlinear frequency shifts, alteration of the fast ion energy distribution, and turbulent energy transfers to shorter length scales. Frequency shifts could provide saturation by altering the basic wave-particle resonance ($\omega = k_{\parallel} v_{\parallel}$) or reducing linear growth rates [$\gamma \propto \beta_{fast}(\omega_{*,fast} - \omega)$]. However, since results both from this model and experiments tend to show that the TAE retains a fairly coherent frequency spectrum throughout its evolution, this avenue of stabilization seems unlikely. Modification of the fast ion energy distribution has been observed as a saturation mechanism for the KAW (kinetic Alfvén wave)[14] in a shearless slab particle model. Steepening of the fast ion distribution can enhance Landau damping of the wave on the fast ions and lower growth rates. In a gyrofluid model the analogous mechanism could be analyzed by including the fast ion

temperature evolution. Work is currently underway on this area. Treatment of the effect of turbulent energy transfers requires resolution of an adequate inertial regime where damped modes are present. As mentioned earlier, this can be problematical for the TAE due the range of toroidal mode numbers which can be unstable. Work is currently underway using q(r) profiles of restricted range in order to limit the width of the wedge in m, n space which must be kept.

In Figs. 10 and 11 we show the evolution of the n = 0, m = 0 components of density, poloidal flux, potential, and parallel velocity for the TFTR beam-driven TAE case described earlier. Fig. 10(a) shows the profile flattening effect of the (0,0) density on the equilibrium fast ion density (plotted here in terms of the gradient to magnify the effect). Fig. 10(b) shows the modifications to the q(r) profile caused by the (0,0) component of poloidal flux. Fig. 11(a) shows the (0,0) potential which results in the poloidal $\vec{E} \times \vec{B}$ velocity plotted in Fig. 11(b). Finally, in Fig. 11(c) the (0,0) parallel fast ion velocity moment is shown. The parallel velocity moment and electrostatic potential are initially zero while the density and poloidal flux initially have non-zero equilibrium values. These (0,0) components are then incorporated back into a linear gyrofluid stability calculation which adds the density and poloidal flux with the pre-existing equilibrium values and includes the appropriate terms for a non-zero potential and parallel velocity. The results of this calculation provide, in effect, an instantaneous linear growth rate diagnostic during the nonlinear evolution; this is of use in understanding the influence of the (0,0) components on saturation. In Fig. 12 such linear growth rates are plotted as a function of time for the various n's. As can be seen, near the point where the nonlinear quantities begin to turn over at $t \cong (500-600)\tau_{Hp}$ [see Fig's. 6(a), 7(a)] the linear growth rates begin to drop, indicating that the (0,0) components are dominant in causing the stabilization. Next, in Figs. 13 and 14 we diagnose this further by turning on and off the various field quantities individually at the point $t = 800\tau_{Hp}$. The top solid curve shows the initial (time = 0) growth rates. The bottom dotted curve shows the growth rates with all (0,0) field quantities included. The chain-dashed curve shows the effect of individual (0,0) fields included. As may be seen from Figs. 13(a) and 13(b), the density and parallel velocity have relatively little effect. The dominant cause of the stabilization comes from the poloidal flux (which induces changes in the q(r) profile) and the potential (which leads to sheared velocity flows).

V. Conclusions

We have developed a gyro-Landau fluid model of the TAE instability which includes many of the growth and damping mechanisms of relevance to this mode. This has been applied to the TFTR and DIII-D beam-driven TAE experiments, as well as to the future DT break-even regime in TFTR. The model provides mode number and frequency spectra which are in the same ranges as the experimental observations. In the case of the DT experiments it indicates that the effect of the high ion temperatures and background plasma β's will tend to quench the alpha-driven TAE instability. However, if the ion temperature can be lowered, more significant growth rates can be obtained.

A primary motivation behind the gyrofluid model is that it is one of the few approaches which can yield information on the nonlinear evolution of the TAE and the mechanisms for its nonlinear saturation. These have been examined here for the TFTR beam-driven case, taking into account the effect of the evolving m,n = (0,0) field quantities. This analysis has shown that the (0,0) components can account for a large fraction of the nonlinear stabilization. A further examination of the effect of individual field quantities (i.e., density, potential, magnetic flux, and parallel velocity) has indicated that the stabilization predominantly arises from the (0,0) potential and poloidal magnetic

flux. The potential results in sheared velocity flows which can decorrelate and break-up the mode structure. The (0,0) poloidal magnetic flux causes small modifications in the q-profile which can influence the continuum damping of the TAE mode.

Acknowledgments

It is a pleasure to acknowledge many useful comments and encouragement from D. J. Sigmar and J.-N. Leboeuf throughout this work.

References

1. K. L. Wong, R. J. Fonck, S. F. Paul, D. R. Roberts, E. D. Fredrickson, R. Nazikian, H. K. Park, M. Bell, N. L. Bretz, R. Budny, S. Cohen, G. W. Hammett, F. C. Jobes, D. M. Meade, S. S. Medley, D. Mueller, Y. Nagayama, D. K. Owens, and E. J. Synakowski, Phys. Rev. Lett. **66,** 1874 (1991).

2. W. W. Heidbrink, E. J. Strait, E. Doyle, G. Sager, and R. Snider, Nuc. Fusion **31**, 1635 (1992).

3. R. Jaenicke, A. Weller, H. J. Hartfuss, A. Lazaros, S. Sattler, H. Zohm, W7-AS Team, Fourteenth International Conference on Plasma Physics and Controlled Fusion Research, IAEA-CN-56/C-2-1, Würzburg, Germany (1992).

4. J. R. Wilson, J. C. Hosea, R. Majeski, C. K. Phillips, J. H. Rogers, G. Schilling, J. E. Stevens, G. Taylor, and the TFTR Group, Bull. Am. Phys. Soc. **37**, 1380 (1992).

5. D. A. Spong, B. A. Carreras, C. L. Hedrick, Phys. Fluids B **4**, 3316 (1992).

6. C. L. Hedrick, J.-N. Leboeuf, Phys. Fluids B **4**, 3915 (1992).

7. C. L. Hedrick, J.-N. Leboeuf, D. A. Spong, Phys. Fluids B **4**, 3869 (1992).

8. R. V. Budny, et al., Nuclear Fusion **32**, 429 (1992).

9. G. Y. Fu, J. W. Van Dam, Phys. Fl. B **1**, 1949 (1989).

10. L. Chen, F. Zonca, Bull. Am. Phys. Soc. **37**, 1436 (1992).

11. S. Zweben, R. Budny, et al., TFTR D-T Experimental Proposal, May 6, 1993.

12. C. T. Hsu, D. J. Sigmar, Phys. Fl. B **4**, 1492 (1992).

13. D. J. Sigmar, F. Gang, R. Gormley, C. T. Hsu, D. A. Spong, Plasma Phys. **34**, 1845 (1992).

14. F. Gang, D. J. Sigmar, J.-N. Leboeuf, Phys. Lett. **A 161** (1992).

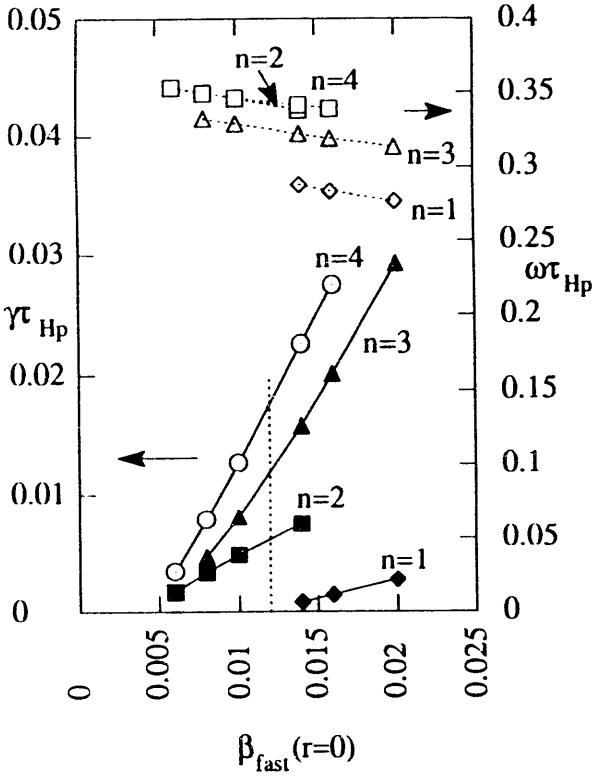

Figure 1(a)

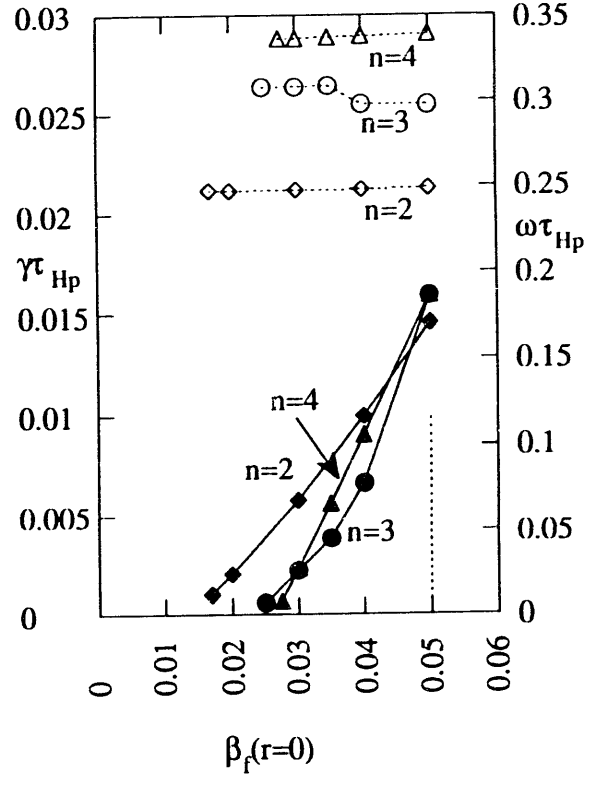

Figure 1(b)

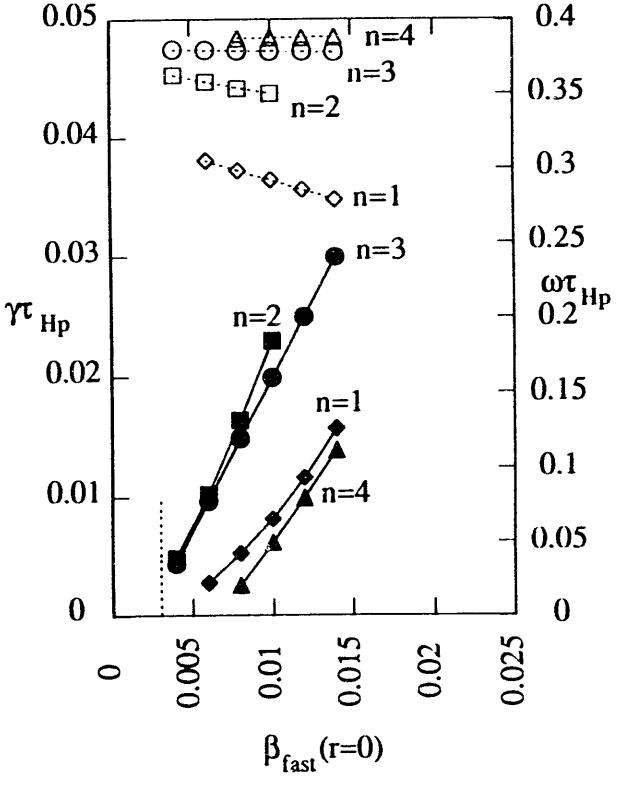

Figure 1(c)

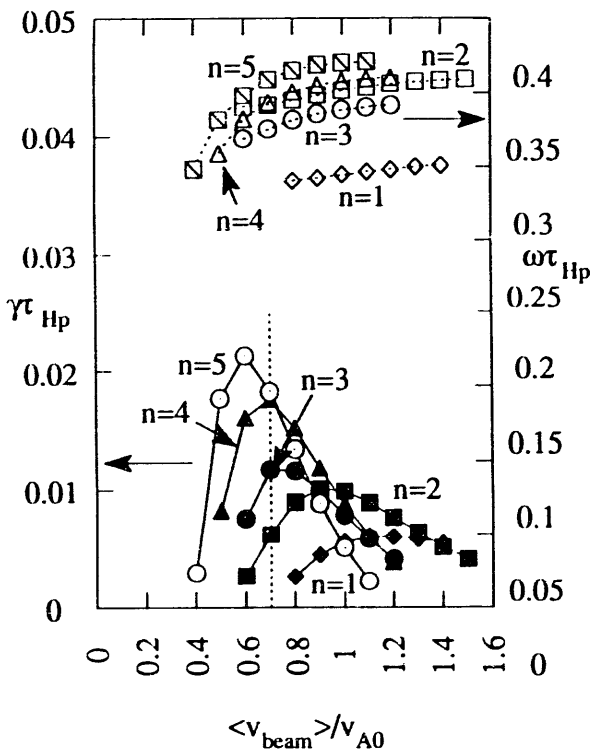

Figure 2(a)

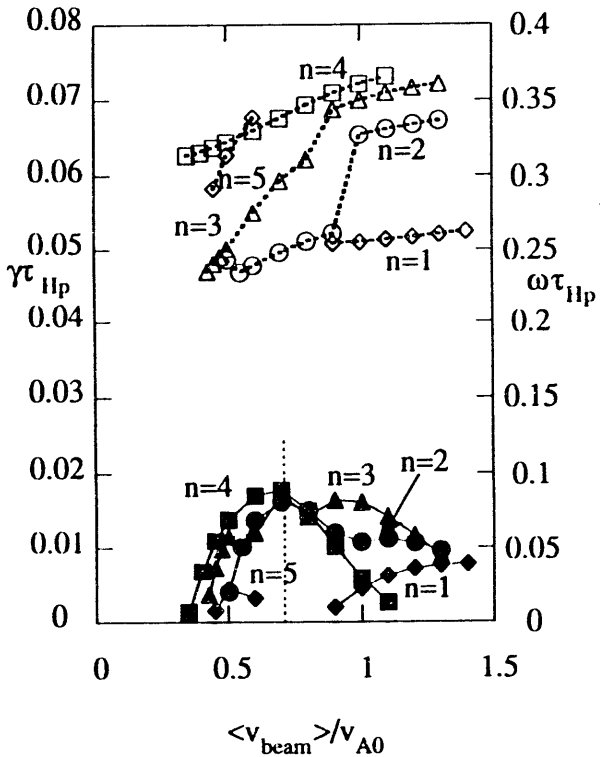

Figure 2(b)

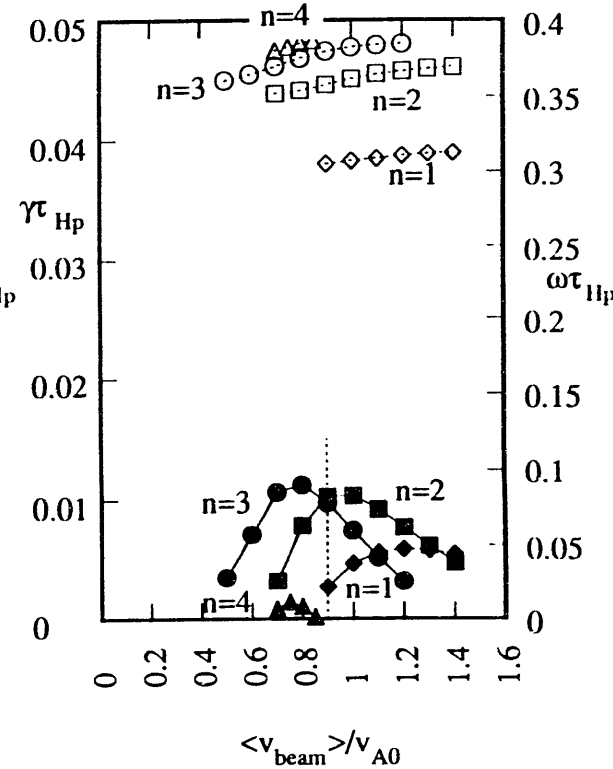

Figure 2(c)

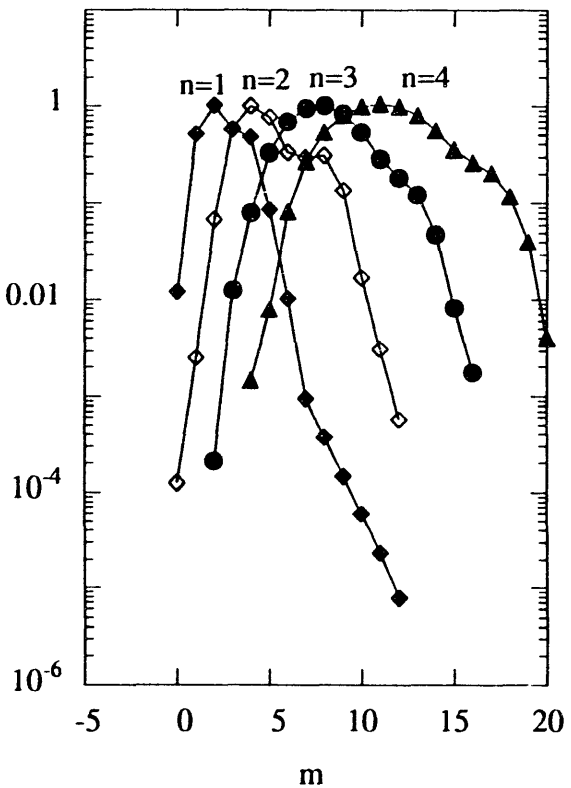

Figure 3(a)

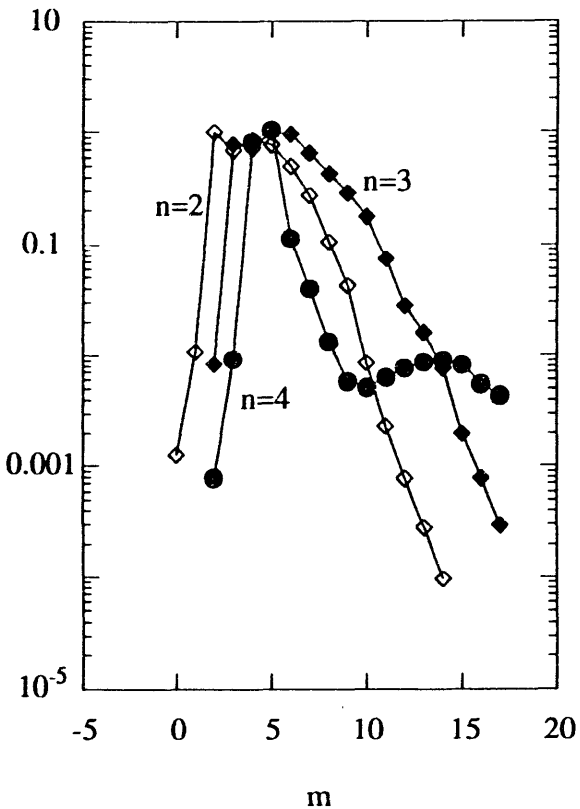

Figure 3(b)

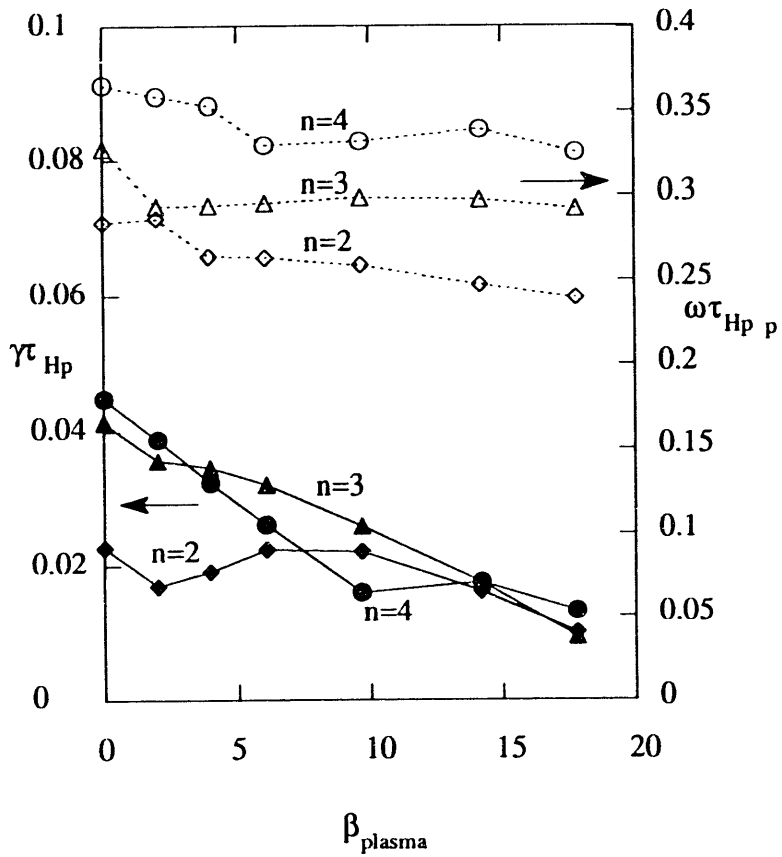

Figure 4

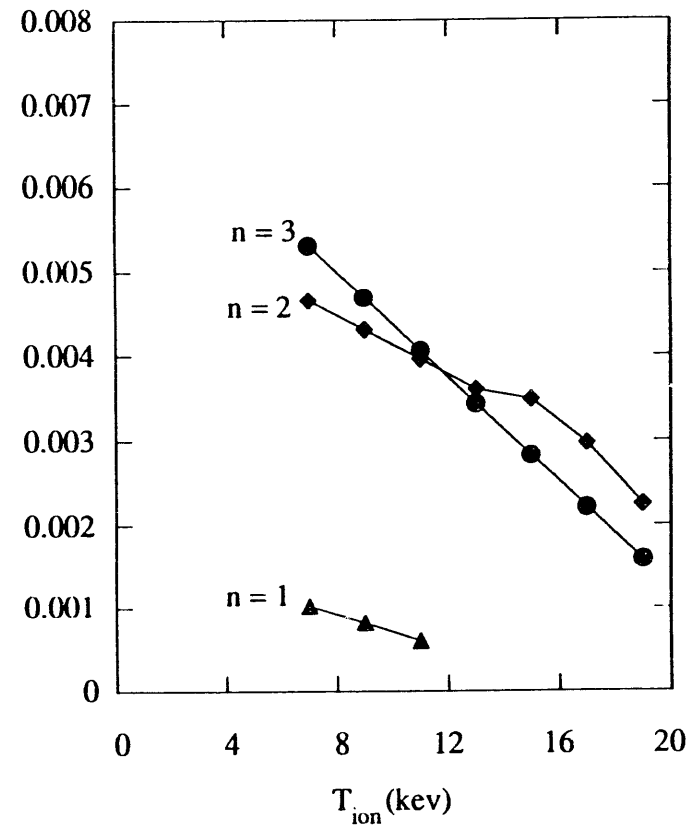

Figure 5

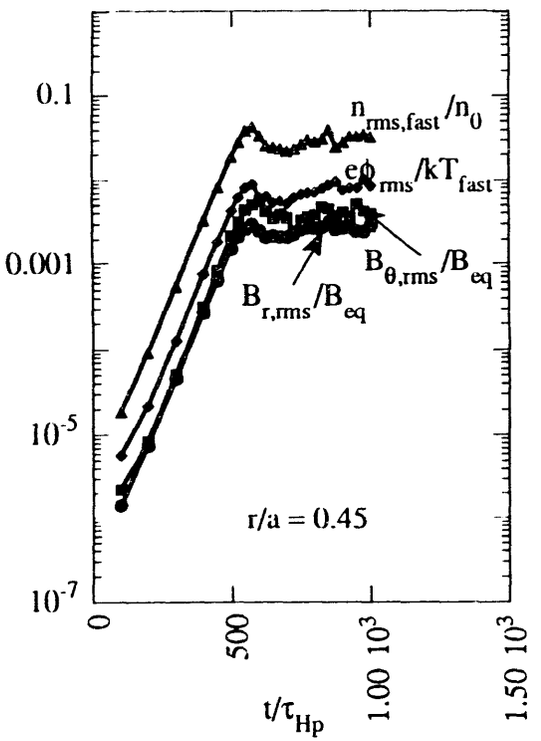

Figure 6(a)

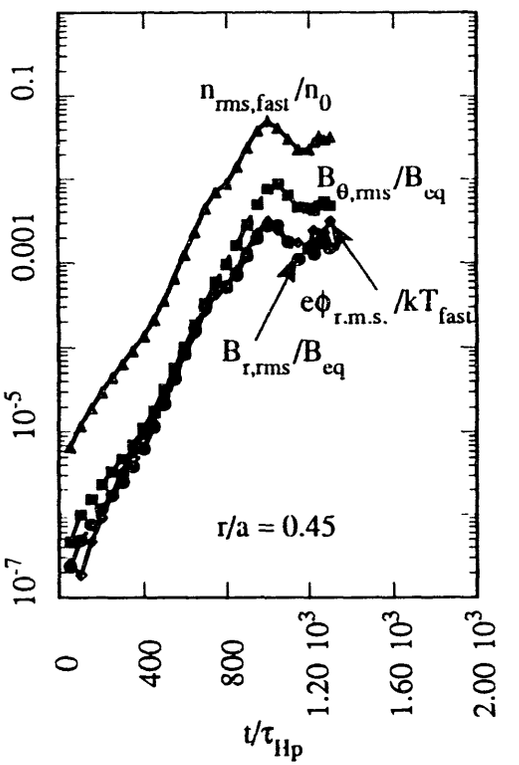

Figure 6(b)

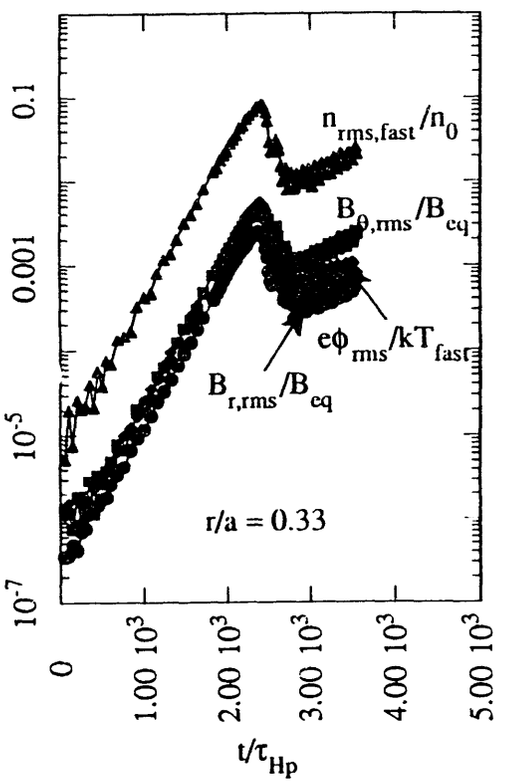

Figure 6(c)

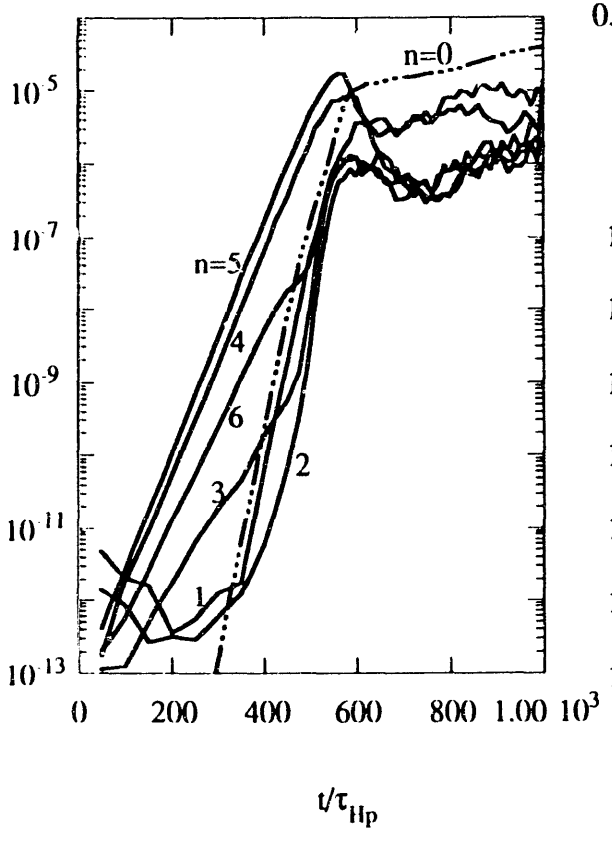

Figure 7(a)

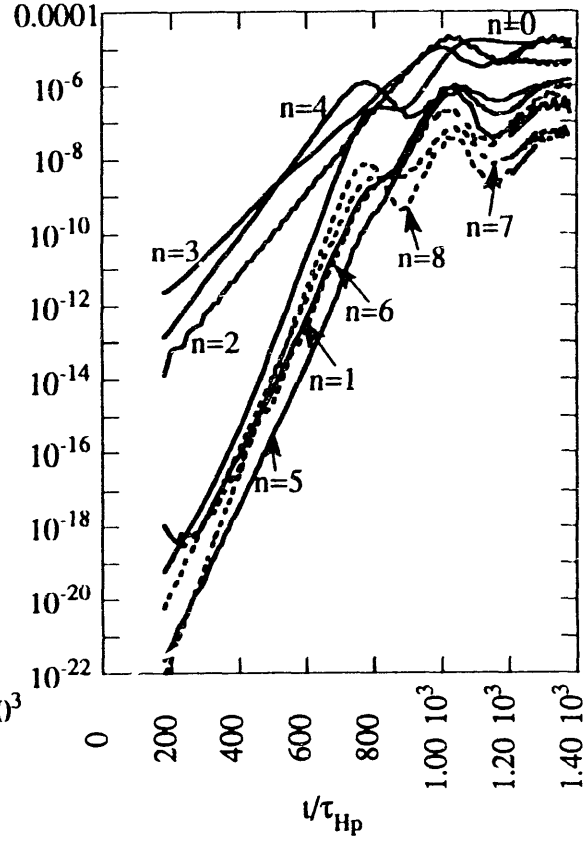

Figure 7(b)

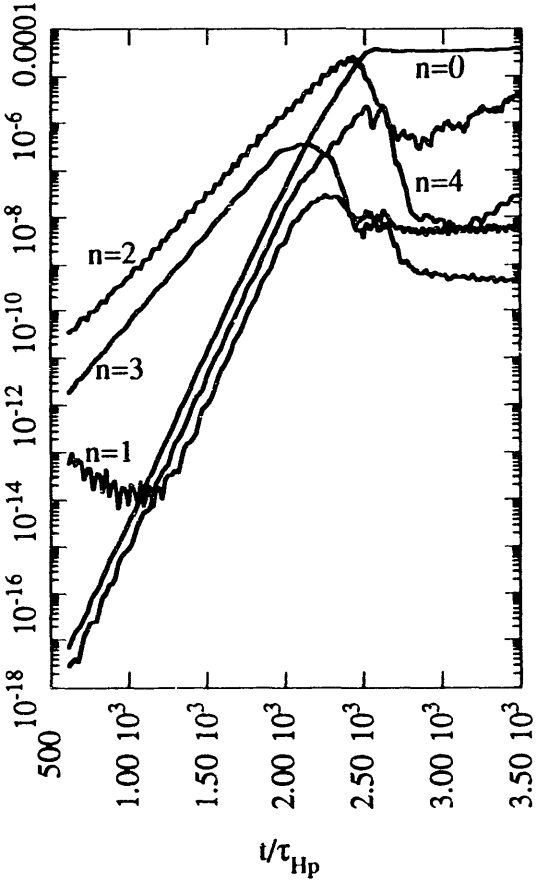

Figure 7(c)

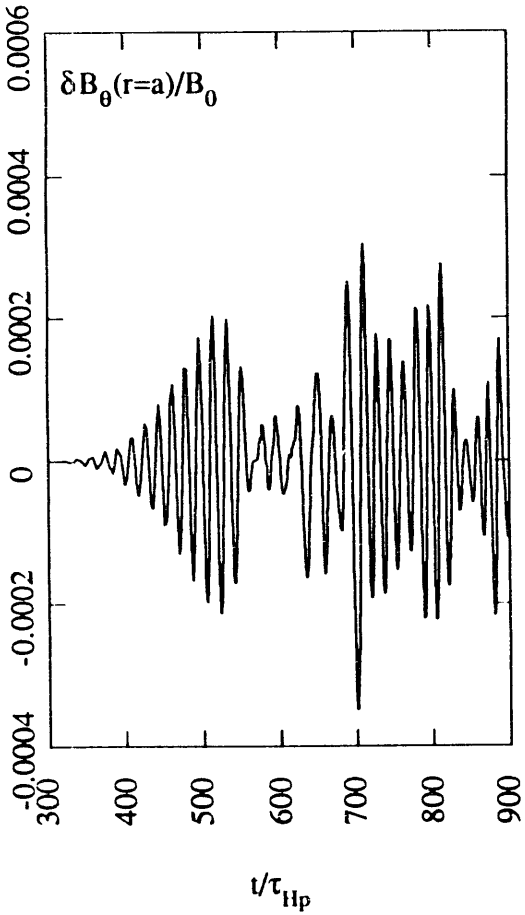

Figure 8(a)

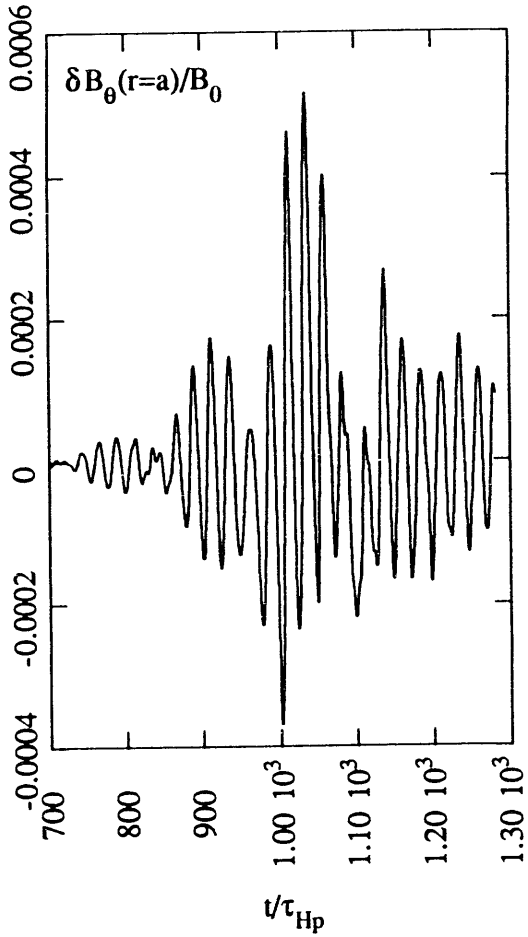

Figure 8(b)

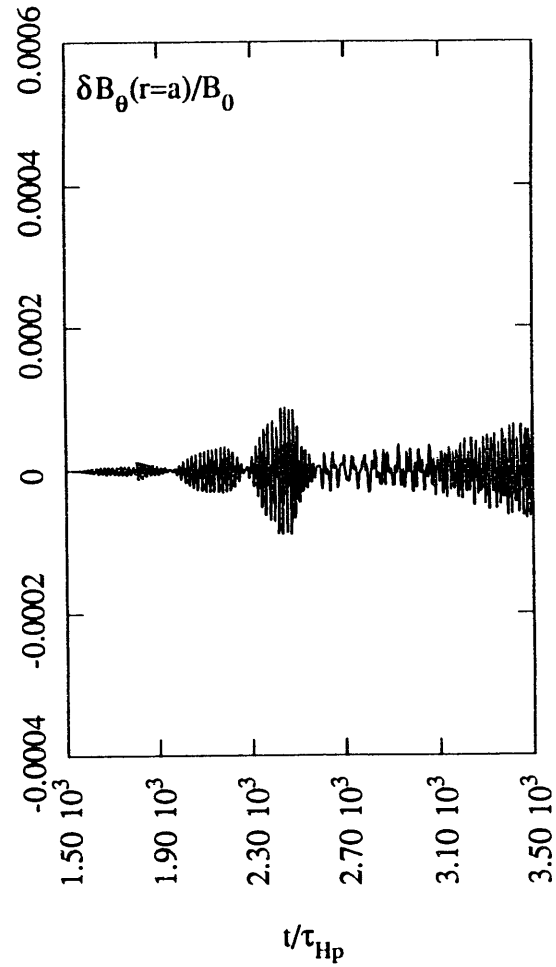

Figure 8(c)

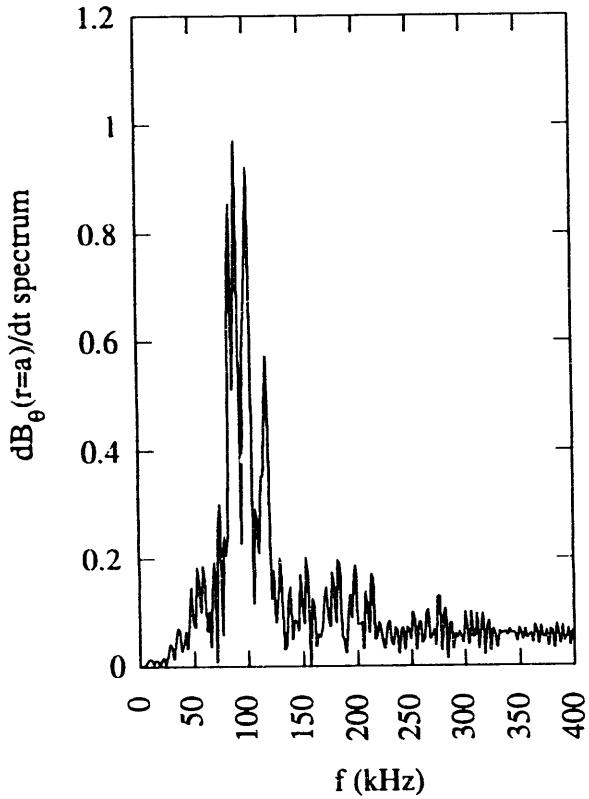

Figure 9(a)

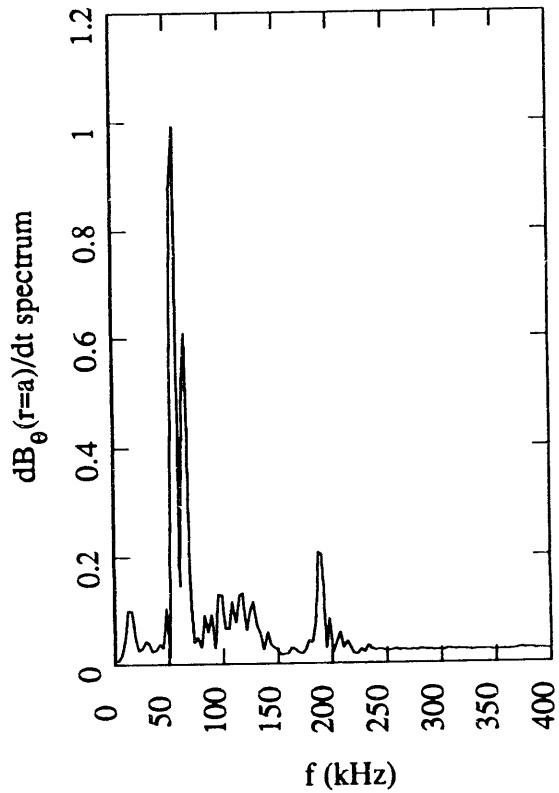

Figure 9(b)

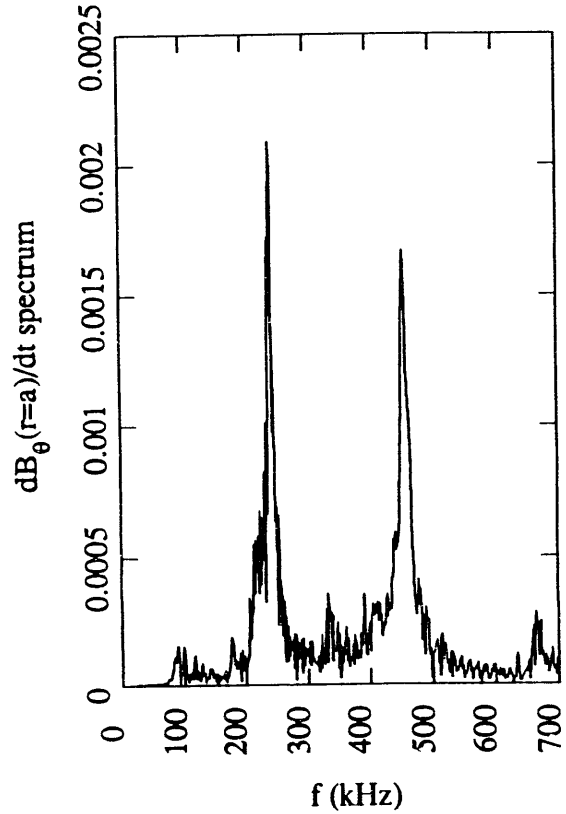

Figure 9(c)

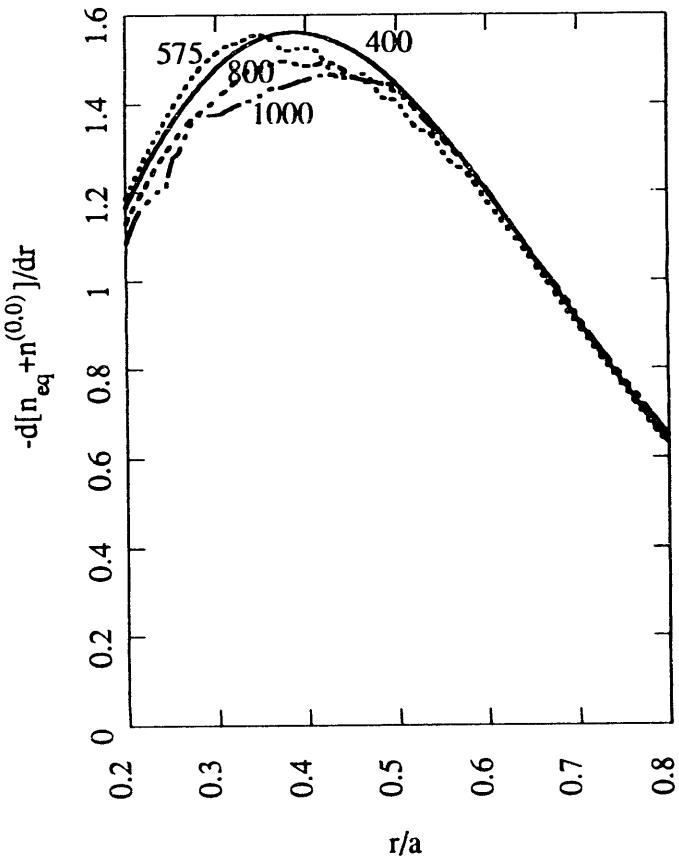

Figure 10(a)

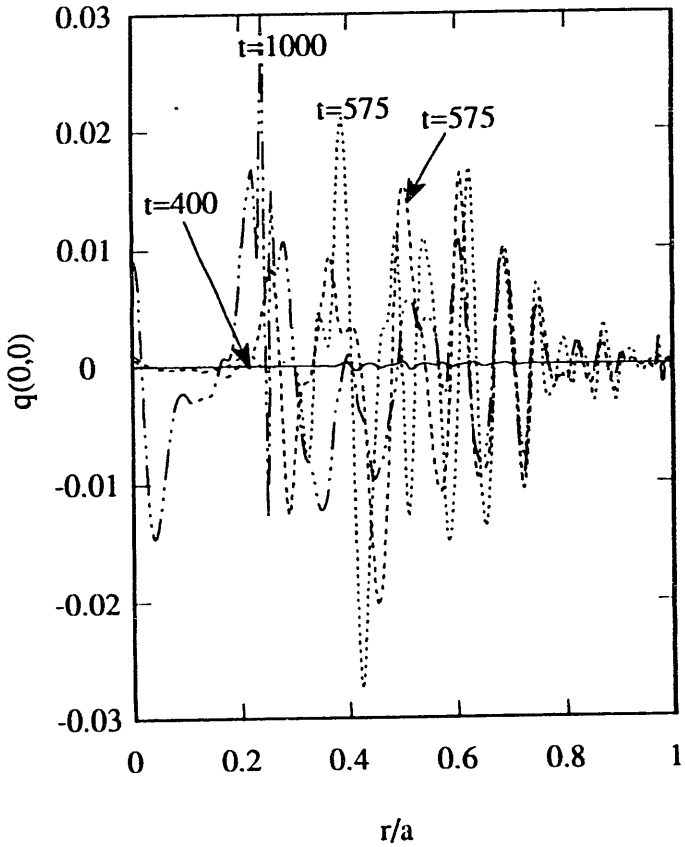

Figure 10(b)

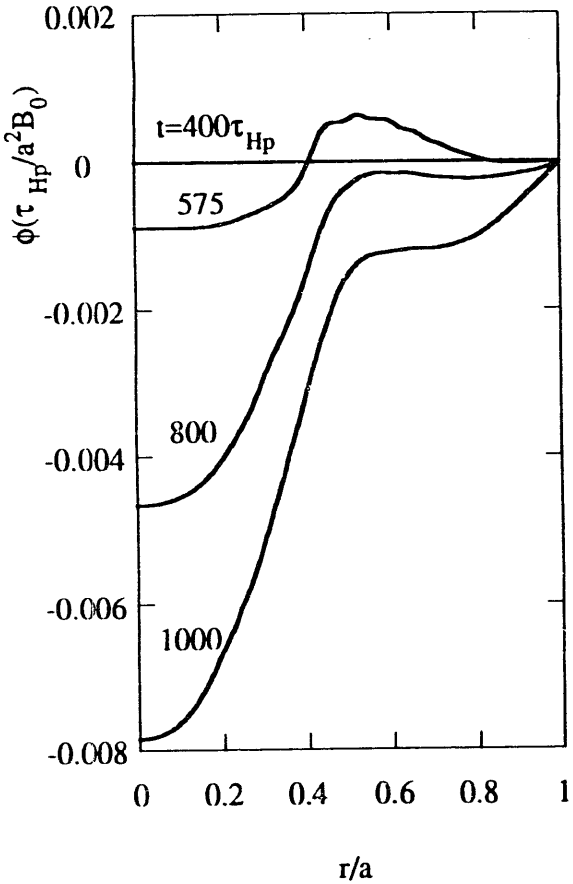

Figure 11(a)

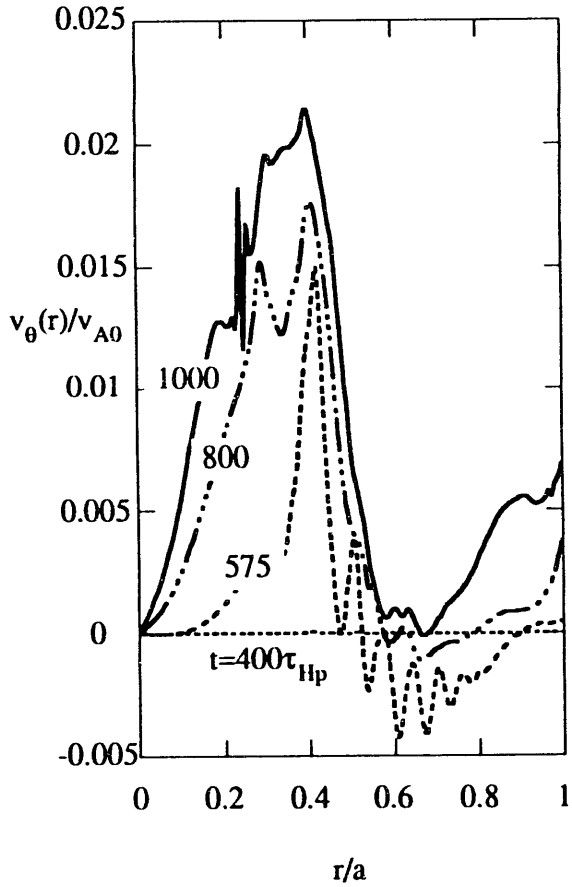

Figure 11(b)

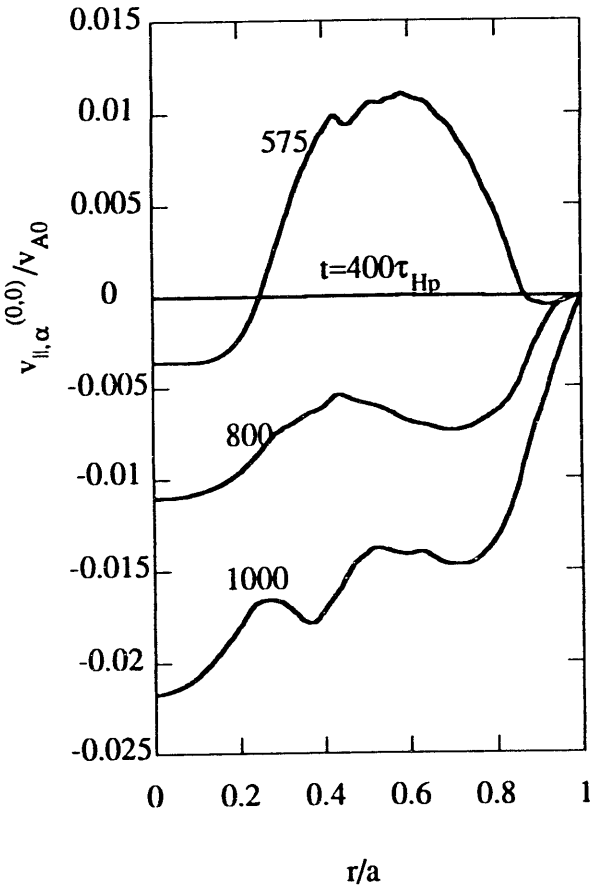

Figure 11(c)

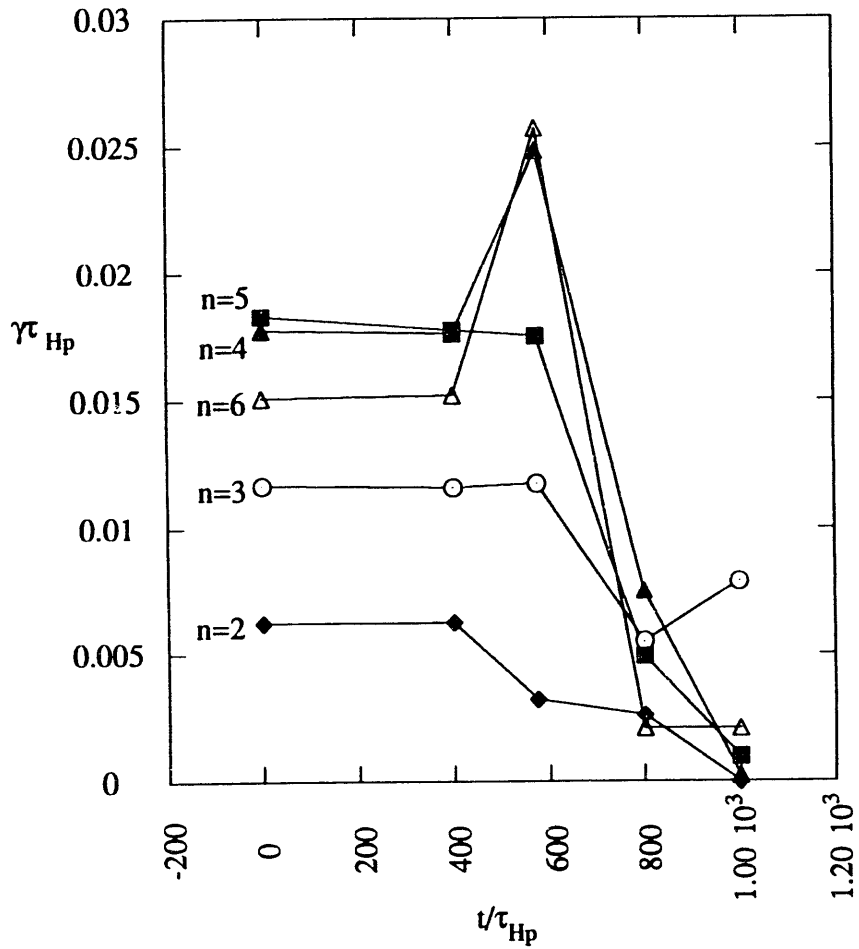
0.03
0.025
0.02
0.015
0.01
0.005
0
$\gamma\tau_{Hp}$
n=5
n=4
n=6
n=3
n=2
-200
0
200
400
600
800
1.00 10^3
1.20 10^3
t/τ_{Hp}

Figure 12

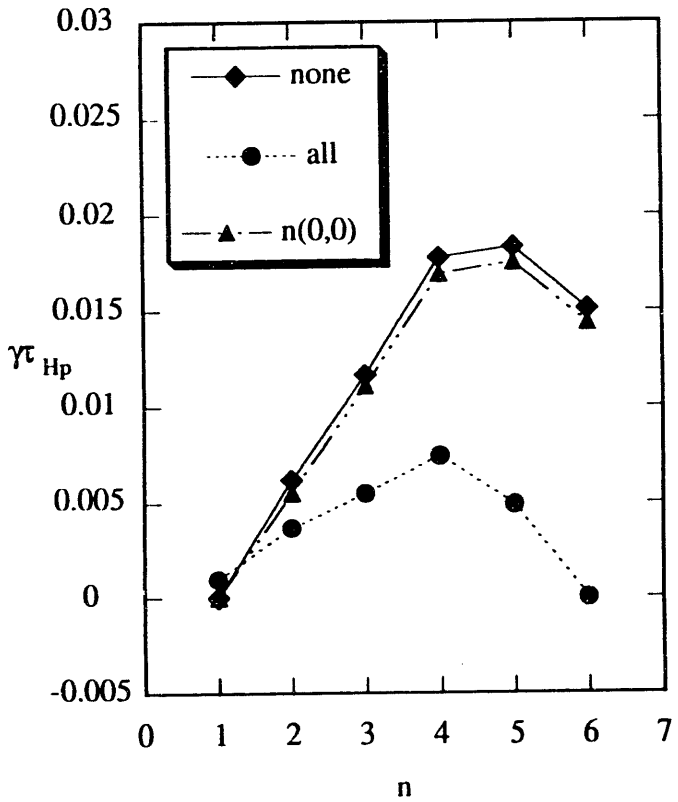

Figure 13(a)

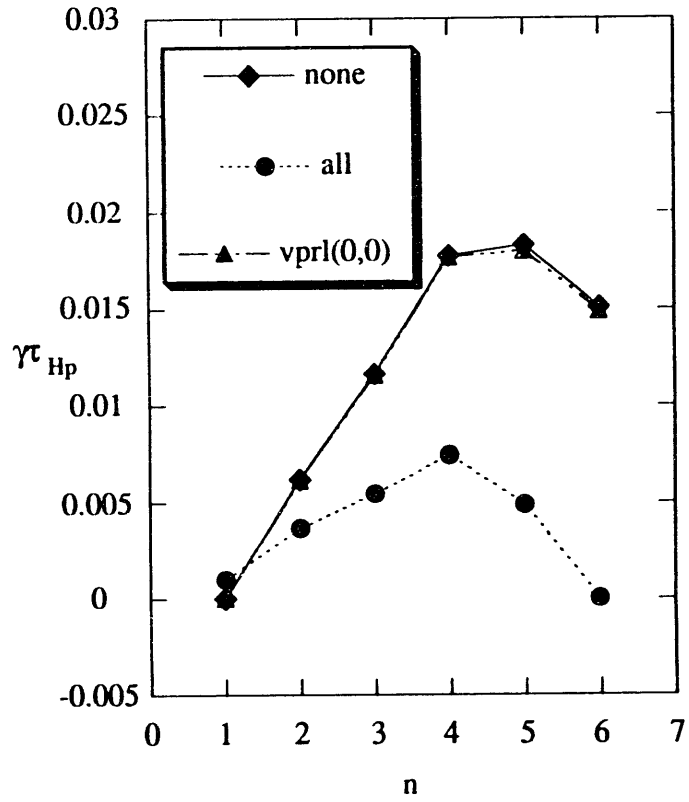

Figure 13(b)

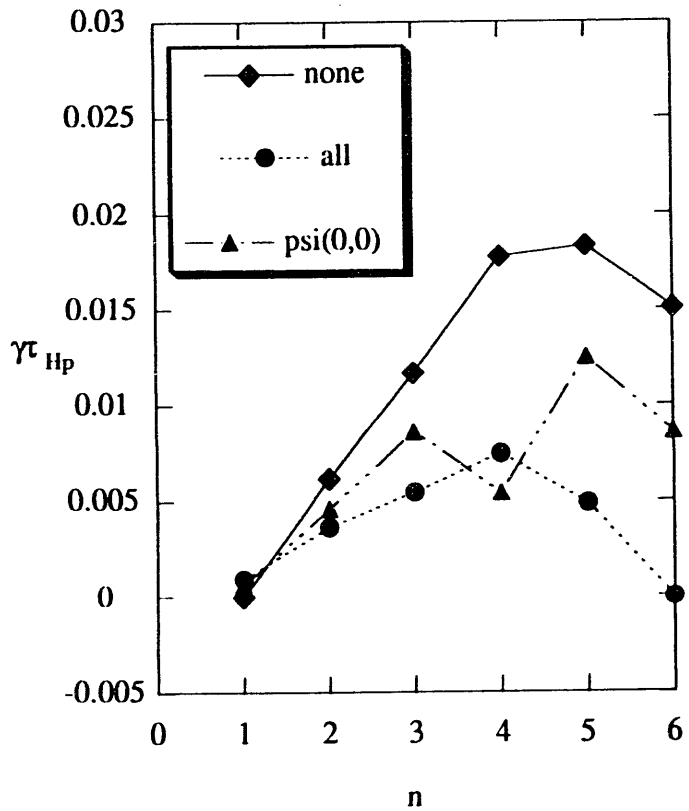

Figure 14(a)

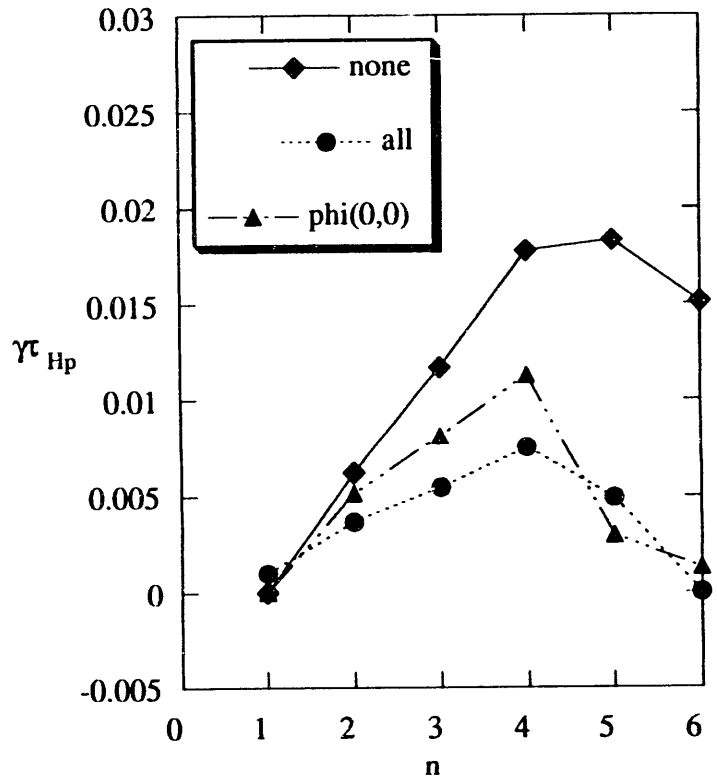

Figure 14(b)

END

DATE
FILMED
8/18/93